GRAPHENE

Spectroscopy signatures of electron correlations in a trilayer graphene/hBN moiré superlattice

Jixiang Yang[1]†, Guorui Chen[2,3,4]†, Tianyi Han[1]†, Qihang Zhang[1], Ya-Hui Zhang[5], Lili Jiang[4], Bosai Lyu[2], Hongyuan Li[3,4], Kenji Watanabe[6], Takashi Taniguchi[6], Zhiwen Shi[2], Todadri Senthil[1], Yuanbo Zhang[7,8], Feng Wang[3,4,9], Long Ju[1]*

ABC-stacked trilayer graphene/hexagonal boron nitride moiré superlattice (TLG/hBN) has emerged as a playground for correlated electron physics. We report spectroscopy measurements of dual-gated TLG/hBN using Fourier transform infrared photocurrent spectroscopy. We observed a strong optical transition between moiré minibands that narrows continuously as a bandgap is opened by gating, indicating a reduction of the single-particle bandwidth. At half-filling of the valence flat band, a broad absorption peak emerges at ~18 milli–electron volts, indicating direct optical excitation across an emerging Mott gap. Similar photocurrent spectra are observed in two other correlated insulating states at quarter- and half-filling of the first conduction band. Our findings provide key parameters of the Hubbard model for the understanding of electron correlation in TLG/hBN.

Moiré superlattices of two-dimensional (2D) materials (1–4) offer a versatile platform to engineer and study correlated electron physics. With additional experimental knobs such as the composition, the twisting angle, and gate electric fields, the electronic band structure and charge density can be (in situ) independently controlled in these synthetic quantum materials. As a result, superconductivity (5–10), correlated insulating states (11–18), orbital magnetism (19), and correlated Chern insulators (12, 20) have been observed in 2D moiré superlattices. Many intriguing questions arise from these observations, such as the nature of correlated insulating states and the mechanism of superconductivity, which call for systematic spectroscopy studies. Although several spectroscopy studies have been carried out (21–26) on the particular system of magic-angle twisted bilayer graphene (MATBLG), experiments on 2D moiré superlattices have been dominated by electron transport measurements. Applying additional top layers for encapsulation (to mimic the dielectric screening of the environment, as in transport experiments) or dual gating (13–17, 27) (relevant to the majority of 2D moiré superlattices) makes

it impossible to use many of the spectroscopic techniques that are commonly used in surface science, such as scanning tunneling spectroscopy and photoemission spectroscopy. To gain a fundamental understanding of the correlated physics in 2D moiré superlattices, developing spectroscopy techniques that can access buried heterostructures is of critical importance at this exciting frontier of research.

Optical transmission and reflection spectroscopy has been widely used to study electronic excitations in conventional strongly correlated materials (28). However, in moiré superlattices, the relevant energy scales of the electronic band and Coulomb gap are substantially smaller (<50 meV) than their counterparts in conventional strongly correlated materials. Consequently, far-infrared spectroscopy with photon wavelengths >25 μm is required to probe correlated electron excitations in moiré superlattices. The corresponding beam spot size (~1 mm when using Globar, the only broadband infrared source) is much larger than that of typical 2D material devices (29), making infrared reflection and transmission spectroscopy of moiré heterostructures extremely challenging. At the same time, infrared absorption in the gate layers easily dominates that from the layer of interest, making it harder to extract a clean signal. So far, no infrared spectroscopy has been applied to top-gated 2D moiré superlattices.

Here, we overcome these challenges by adopting Fourier transform infrared (FTIR)–photocurrent spectroscopy for the optical absorption measurement of an ABC-stacked trilayer graphene/hexagonal boron nitride moiré superlattice (TLG/hBN). The overall methodology is similar to that described in (29). However, a notable improvement of signal-to-noise ratio has been achieved in this study, which enables spectroscopy of correlated states in moiré superlattices (30); we

applied this technique to dual-gated TLG/hBN (as illustrated in Fig. 1A).

Figure 1B shows the calculated band structure of TLG/hBN in the mini-Brillouin zone using a tight-binding model, where a moiré potential exists at the top layer of TLG (30). Dashed curves represent the four lowest moiré minibands at zero displacement field D, where the bandgap at charge neutrality is zero. As we apply a positive (negative) D by controlling bottom- and top-gate voltages, a positive (negative) potential energy difference between the bottom and top graphene layers is induced ($\Delta = E_t - E_b$); the resulting minibands are shown as solid curves. Here, we define the positive direction of D to be pointing from the bottom gate to the top gate. This potential energy asymmetry corresponds to a bandgap that is slightly smaller than $|\Delta|$. The highest valence band is well separated from the other bands, forming an obvious flat band that hosts correlated insulating states when doped (27, 31, 32). The lowest conduction band also features a small bandwidth, but it partially overlaps with the second-lowest conduction band. Interband optical transitions can happen between these moiré minibands, as indicated by arrows I_1 to I_4. I_1 and I_4 have the largest oscillator strengths because they are allowed even in the absence of the moiré potential. By contrast, I_2 and I_3 are allowed only by the moiré potential effect, and they contribute less to optical conductivity. Figure 1C shows the experimental photocurrent spectrum at $D = -0.71$ V/nm, which features a sharp and strong peak at ~72 meV. The photocurrent signal is zero below this peak. There is a second broader peak residing at ~20 meV above the main peak. The sharp peak at ~102 meV is caused by interlayer electron-phonon coupling between hBN and graphene and requires further study.

Using the calculated optical conductivity spectrum in Fig. 1C as a reference, the experimental photocurrent spectrum can be interpreted. The main peak at ~72 meV is dominated by the interband transition I_1 in Fig. 1B, and the second peak at ~95 meV may result from I_3 and I_4 transitions. The separation between these two peaks corresponds to the bandgap between the two valence bands, supporting the important presumption that the highest valence band is isolated when considering correlation effects. The peak width of the main peak is determined by the joint density of states (DOS), which is closely related to the peak width of the van Hove singularities in the DOS (30) of the highest valence band and the lowest conduction band. When both bands are relatively flat as in bandgap-opened TLG, the observed peak width serves as a good indicator of the single-particle bandwidth W.

In contrast to MATBLG, where W is determined mostly by the twisting angle, theory

¹Department of Physics, Massachusetts Institute of Technology, Cambridge, MA, USA. ²Key Laboratory of Artificial Structures and Quantum Control (Ministry of Education), Shenyang National Laboratory for Materials Science, School of Physics and Astronomy, Shanghai Jiao Tong University, Shanghai 200240, China. ³Materials Science Division, Lawrence Berkeley National Laboratory, Berkeley, CA, USA. ⁴Department of Physics, University of California at Berkeley, Berkeley, CA, USA. ⁵Department of Physics, Harvard University, Cambridge, MA, USA. ⁶National Institute for Materials Science, Tsukuba, Japan. ⁷State Key Laboratory of Surface Physics and Department of Physics, Fudan University, Shanghai, China. ⁸Institute for Nanoelectronic Devices and Quantum Computing, Fudan University, Shanghai, China. ⁹Kavli Energy NanoSciences Institute at the University of California, Berkeley, CA, USA.
*Corresponding author. Email: longju@mit.edu
†These authors contributed equally to this work.
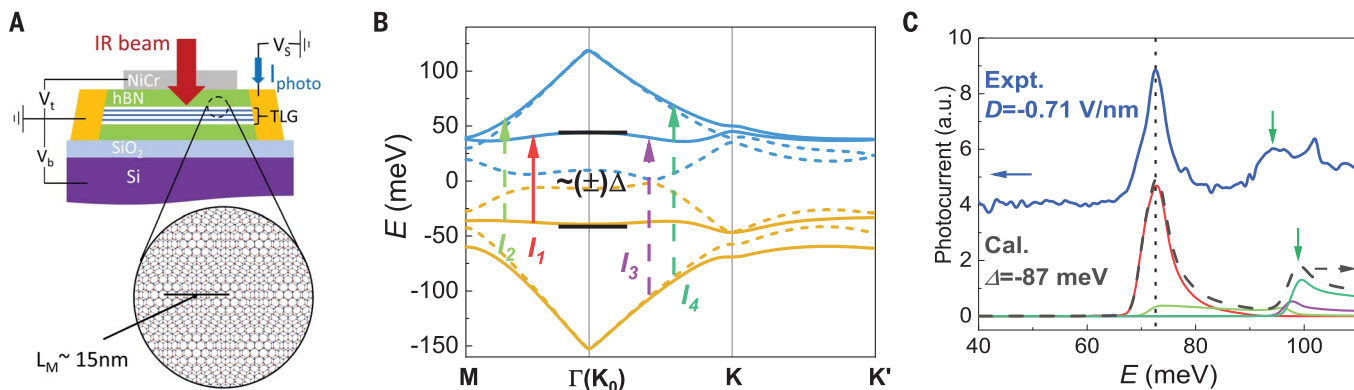
Fig. 1. Device structure and interband optical transitions in an ABC-stacked TLG/hBN moiré superlattice. (**A**) Illustration of a dual-gated TLG device with a moiré wavelength of ~15 nm. IR, infrared; V_b, bottom-gate voltage; V_t, top-gate voltage; V_s, source-drain voltage. (**B**) Calculated band structure of TLG in the mini-Brillouin zone under a moiré potential (30). Dashed curves represent minibands at zero displacement field, whereas solid curves indicate minibands at a displacement field induced by gates so that $\Delta = -87$ meV. Δ represents the gate-induced potential difference between the top and bottom layer of TLG. Arrows labeled as I_1 to I_4 represent interband optical transitions when the Fermi level is inside the gap. (**C**) The photocurrent spectrum of TLG/hBN at a displacement field $D = -0.71$ V/nm and calculated optical conductivity spectrum at $\Delta = -87$ meV. Calculated contributions from transitions I_1 to I_4 are plotted as solid curves, and the sum is plotted as a dashed curve. The prominent experimental peak at ~72 meV (indicated by the vertical dashed line) corresponds to transition I_1. The peak in the photocurrent spectrum indicated by a green arrow corresponds to the peak in optical conductivity that is dominated by I_3 and I_4. All photocurrent spectroscopy measurements were performed at a sample temperature of 2 K. a.u., arbitrary units; Cal., calculated; Expt., experimental.

predicts that the moiré bandwidth in TLG/hBN can be tuned in situ by D (32). Our measurement allows a direct visualization of this electrical tuning of the moiré flatband bandwidth. Figure 2A shows photocurrent spectra of TLG/hBN at several values of D, where the charge density is fixed at zero. At $D = -0.38$ V/nm, the spectrum features a broad peak at ~35 meV with a full width at half-maximum (FWHM) of ~20 meV. This wide peak width is caused by the relative dispersive bands at small displacement fields. As D changes from −0.38 to −0.55 to −0.71 V/nm, this peak blue-shifts and quickly sharpens monotonically. At positive D and Δ, a similar broad peak is observed at $D = 0.33$ V/nm. This peak sharpens at $D = 0.49$ V/nm and eventually broadens again at $D = 0.66$ V/nm, showing a nonmonotonic change of peak width. At the same time, a second peak corresponding to I_3 and I_4 emerges gradually as $|D|$ increases in both directions. Such trends are better seen in the color plot of the photocurrent spectra in Fig. 2B when D is continuously tuned. Dashed lines correspond to the spectra in Fig. 2A with the same color. We calculated optical conductivity spectra as a function of D, as shown in Fig. 2C. By aligning the lowest-energy peak position in both the experimental photocurrent spectrum and the calculated optical conductivity spectrum, we established a conversion from D to Δ (30). This allowed us to outline two regions by white boxes in Fig. 2C that correspond to the experimental data in Fig. 2B. Major features and trends in Fig. 2B are well reproduced by calculation in Fig. 2C. The blue shift of the I_1-dominated optical transition peak indicates the opening of the bandgap. At the same time,

the bandwidth of the relevant moiré bands continuously evolves.

Figure 2D summarizes the FWHM of the I_1-dominated peak as a function of Δ. Both experimental and calculated FWHM decrease monotonically to ~5 meV as Δ moves in the negative direction. With $\Delta > 0$, a minimum FWHM of ~7 meV is observed experimentally at $\Delta \sim 60$ meV. The calculated peak width of the DOS of the highest valence band (30) is plotted as blue diamonds. It shows a trend similar to that of the optical transition peak FWHM, reaching a minimum of 5 meV. The evolution of the optical transition peak width largely reflects that of the bandwidth W of the highest valence band, which is plotted as green triangles. As the bandgap is opened, the bandwidth W is suppressed and eventually approaches ~12 meV. This value is smaller than the estimated on-site Coulomb repulsion energy $U = \frac{e^2}{4\pi\varepsilon_0\varepsilon l_M} \approx 25$ meV (where $l_M = 15$ nm is the moiré wavelength, and $\varepsilon = 4$ is the dielectric constant of hBN), making correlation effects possible when partial doping is induced by gates. Our data also indicated a slightly broader peak width at $\Delta > 0$ than at $\Delta < 0$ for the whole range (30). This observed asymmetry of peak width implies a bigger W for the $\Delta > 0$ side, which agrees with the fact that correlation effects are stronger at negative D than at positive D in transport experiments (8) as well as with the theoretical calculation of bandwidth W, as shown in Fig. 2D.

Next, we examine optical transitions in the correlated insulating state when the flat valence band is doped. Figure 3A shows the device resistance as a function of top- and

bottom-gate voltages. At half-filling of the flat valence band ($\nu = -\frac{1}{2}$), a correlated insulating state is formed, as indicated by a resistance peak. Figure 3B shows the photocurrent spectrum at zero-filling of this hole band at $D = -0.44$ V/nm, where a photocurrent peak centered at 45 meV corresponds to I_1, as illustrated by the inset. This peak has a FWHM of ~13 meV; the calculations in Fig. 2D predict a DOS peak width of 10 meV at this D. At $\nu = -\frac{1}{2}$ with a similar displacement field $D = -0.42$ V/nm, the photocurrent spectrum is dramatically changed, as shown in Fig. 3C. We observed a new strong peak centered at ~18 meV. This energy is clearly below the bandgap energy in Fig. 3B, yet it is bigger than the DOS peak width of the flat valence band. The FWHM of this new peak is ~18 meV, which is substantially broader than the peak width in Fig. 3B. The I_1-dominated peak is merged into the broad background.

These observations at $\nu = -\frac{1}{2}$ all point to a picture that is much more complicated than that in a doped band insulator, where electron correlation effects can be neglected. For a half-doped single-band Hubbard model, theoretical calculations (33–35) predicted a broad peak in the optical conductivity spectrum centering around on-site Coulomb repulsion energy U. Such features have been observed by optical spectroscopy experiments in conventional strongly correlated materials (33, 36, 37). We believe that the strong peak at 18 meV in Fig. 3C indicates the formation of upper and lower Hubbard bands with an optical excitation across the Mott gap, as illustrated by the inset of Fig. 3C. In the final state of this optical excitation, a hole is left at one site

Fig. 2. Displacement field–dependent interband optical transitions at zero doping. (**A**) Photocurrent spectra at several representative displacement fields and zero doping at 2 K. The spectra are shifted vertically for clarity. At $D = -0.38$ V/nm, the low-energy peak is very broad in energy, indicating a large dispersion of both conduction and valence bands. As D becomes more negative and the bandgap increases, this peak blue-shifts and narrows, indicating that the lowest conduction and valence bands are being squeezed by the bandgap. At positive D, the peak position also blue-shifts monotonically, whereas the peak width first narrows and then broadens. (**B**) The 2D color plot of the photocurrent (P.C.) spectra as a function of D. Dashed lines correspond to the spectra in (A) with the same colors. (**C**) The 2D color plot of the calculated optical conductivity (O.C.) spectra as a function of Δ. The two white boxes outline the corresponding range of data in (B). A good agreement with (B) is observed for both I_1- and I_4-dominated spectrum ranges. (**D**) FWHM of the I_1-dominated peak as a function of Δ extracted from (B) and (C) are shown as black squares and red dots, respectively. Blue diamonds represent the calculated DOS van Hove singularities peak width of the highest valence band. Green triangles represent the full bandwidth of the highest valence band. As the bandgap is opened, both single-particle DOS peak and optical transition peak widths become considerably narrower, driving the system into a correlated-electron regime when doped. BW, bandwidth; PW, peak width.
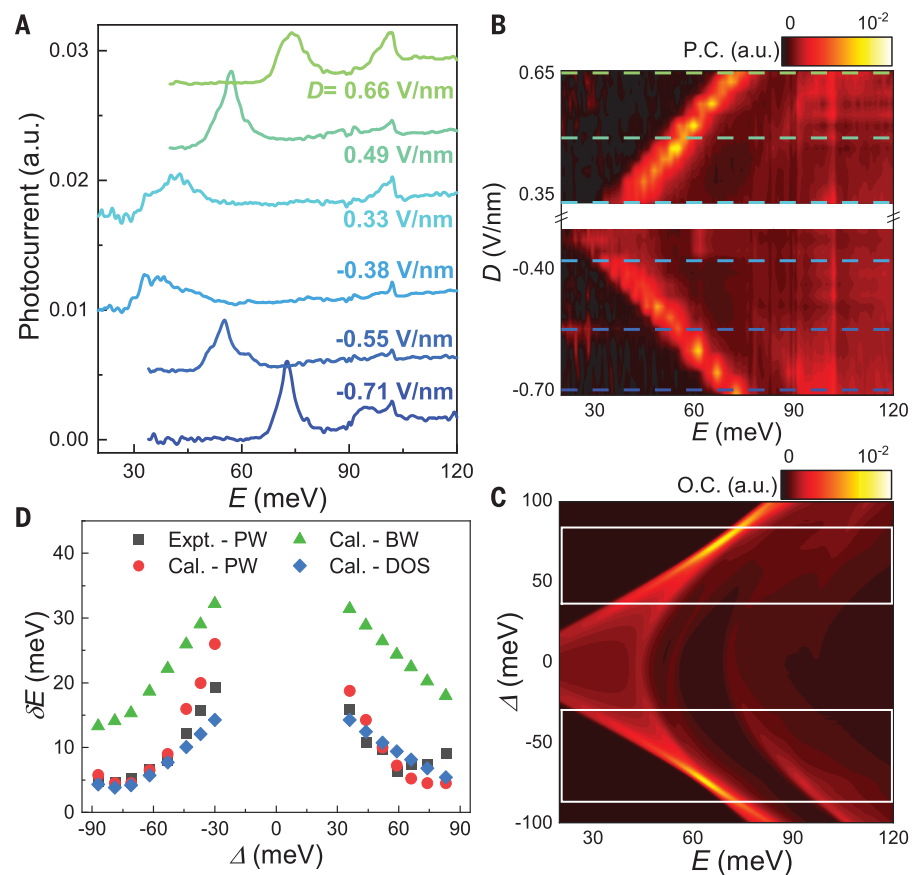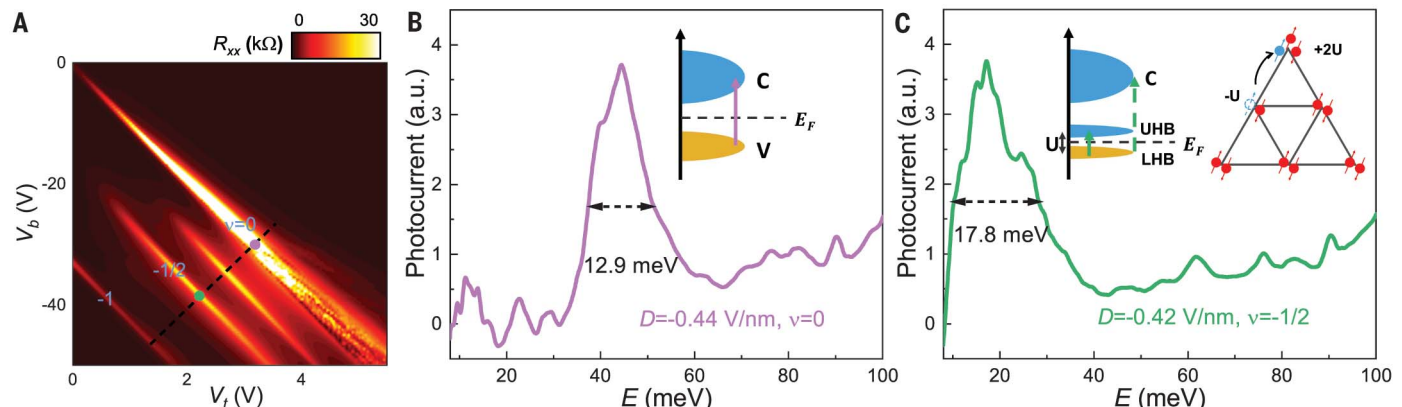

Fig. 3. Optical transitions in the correlated insulating state. (**A**) Device resistance (R) as a function of the top- and bottom-gate voltages. The dashed line indicates the constant D direction. Resistance peaks corresponding to full-filling, half-filling, and zero-filling of the highest valence band are labeled as $\nu = -1$, $-\frac{1}{2}$, and 0, respectively. (**B**) The photocurrent spectrum taken at the purple dot position in (A). The spectrum is dominated by a sharp peak at ~45 meV, which corresponds to the I_1 transition, as illustrated by the inset. C, conduction band; E_F, Fermi energy; V, valence band. (**C**) Photocurrent spectrum taken at the green dot position in (A). In contrast to the spectrum in (B), a broad peak at ~18 meV emerges, corresponding to an optical transition across the Mott gap, as illustrated by the solid arrow in the inset on the left. The final state of such optical excitation contains a hole at one site and an extra electron at another site in the triangular moiré superlattice, as illustrated in the inset on the right. The I_1 peak (indicated by the dashed arrow in the inset on the left) is merged into the background. LHB, lower Hubbard band; UHB, upper Hubbard band. The spectra in (B) and (C) are taken at 2 K.

while an extra electron is added to another site on the triangular moiré superlattice of TLG/hBN. For the moiré superlattice in our device, $\frac{e^2}{4\pi\varepsilon_0\varepsilon l_M} \approx 25$ meV is expected to be a good estimate of the onsite Coulomb repulsion energy U (*38*). This energy is close to the peak position of 18 meV in Fig. 3C. The second piece of evidence of correlation effects is the large broadening of the low-energy peak. The FWMH of 18 meV is several times bigger than expected from the simple uncorrelated band picture: Without correlations, one expects a peak width of ~6.5 meV, as inferred from the experimental spectrum in Fig. 3B, and ~5 meV from calculations. Thirdly, the interband transition from the lower Hubbard band to the lowest conduction miniband (illustrated by the dashed arrow in the inset of Fig. 3C) is difficult to

distinguish from the broad continuous background. It is likely that the DOS distribution of the lowest conduction band, which is remote to the flat valence band, also gets substantially broadened and prevents an easy identification of the transition from the experimental spectrum. The broadening of both the flat band and remote band is similar to what happens in MATBLG (21, 22, 24), indicating that strong correlation effects play a key role in our system.

We now briefly discuss the implication of this low-energy optical transition on the detailed nature of the Mott insulator state at $\nu = -\frac{1}{2}$ of the valence flat band. We can rule out spin- and valley-polarized ferromagnetic ground states, because optical transitions are forbidden in such states owing to the conservation of spin and valley pseudospin. This is also supported by transport measurements where magnetism is absent from the topologically trivial side of TLG/hBN (12). Other candidate ground states such as antiferromagnetic and intervalley-coherent Mott insulators on a triangular lattice (36, 38) allow optical transitions across the charge gap. They both agree with our experimental results, but a more precise identification requires further experimental and theoretical studies. In particular, continuous tuning of Δ and intersite coupling parameters in TLG/hBN facilitate experimental exploration of multiple ground states.

Besides the correlated insulating state at $\nu = -\frac{1}{2}$ of the flat valence band, we also explored magnetic field–induced insulating states when the Fermi level is shifted into the lowest conduction band at $D > 0$. Figure 4A shows the transport signature of such states when D is positive. At zero magnetic field, the device resistance features a single peak corresponding to filling factor $\nu = 0$, whereas the electron-doped side is featureless. However, at magnetic field $B = 7.5$ T, resistance peaks appear at $\nu = \frac{1}{4}$ and $\frac{1}{2}$ of the lowest conduction band. These features mimic the transport signatures of correlated insulating states at $-\frac{1}{4}$ and $-\frac{1}{2}$ filling of the flat valence band when D is negative. Figure 4B shows the photocurrent spectra corresponding to these two new insulating states. At $\nu = 0$, a peak located at ~50 meV indicates interband transition across the displacement field–induced bandgap. By contrast, at quarter- and half-filling, a peak located at ~22 meV emerges and dominates both spectra; no obvious peak can be identified near 50 meV at quarter- and half-filling.

Because $\nu = \frac{1}{4}$ and $\frac{1}{2}$ correspond to one electron and two electrons per site on the moiré superlattice, we believe that these two states are also driven by electron correlation, as in the Mott insulator state of the flat valence band at $\nu = -\frac{1}{2}$. The exact role of the magnetic field is to be clarified by further measurements. Phenomenologically, the peak positions and widths in photocurrent spectra at these two magnetic field–induced insulating states are similar to those of the peak in Fig. 3C. We believe that a correlation-driven band splitting similar to that in Fig. 3C is present in this scenario, as illustrated by the inset of Fig. 4B. In both cases, the optical excitation energy is largely determined by the onsite Coulomb repulsion energy U, which is set by the same moiré wavelength and independent of the displacement field and the doping type.

Our measurements provide spectroscopic evidence of electron correlation effects in a TLG/hBN moiré superlattice. We have experimentally determined energy scales for relevant parameters of the Hubbard model, which form a basis for accurate theoretical modeling and understanding of both observed (8, 12, 27) and predicted correlated ground states (36–38) in this moiré superlattice. These observations open up opportunities to explore the doping and temperature dependence of the optical spectrum, sum rules for optical conductivity (28, 33), and bound excitons of holon and doublon (28, 39), which all call for further systematic study and theoretical calculations. The FTIR photocurrent spectroscopy technique used here can be readily generalized to other encapsulated and (dual-)gated 2D moiré superlattice devices for a better understanding of correlated electron physics in this designer material platform.

REFERENCES AND NOTES

1. M. Yankowitz et al., Nat. Phys. 8, 382–386 (2012).
2. C. R. Dean et al., Nature 497, 598–602 (2013).
3. L. A. Ponomarenko et al., Nature 497, 594–597 (2013).
4. B. Hunt et al., Science 340, 1427–1430 (2013).
5. Y. Cao et al., Nature 556, 43–50 (2018).
6. M. Yankowitz et al., Science 363, 1059–1064 (2019).
7. X. Lu et al., Nature 574, 653–657 (2019).
8. G. Chen et al., Nature 572, 215–219 (2019).
9. J. M. Park, Y. Cao, K. Watanabe, T. Taniguchi, P. Jarillo-Herrero, Nature 590, 249–255 (2021).
10. Z. Hao et al., Science 371, 1133–1138 (2021).
11. Y. Cao et al., Nature 556, 80–84 (2018).
12. G. Chen et al., Nature 579, 56–61 (2020).
13. X. Liu et al., Nature 583, 221–225 (2020).
14. Y. Cao et al., Nature 583, 215–220 (2020).
15. S. Chen et al., Nat. Phys. 17, 374–380 (2021).
16. E. C. Regan et al., Nature 579, 359–363 (2020).
17. Y. Tang et al., Nature 579, 353–358 (2020).
18. L. Wang et al., Nat. Mater. 19, 861–866 (2020).
19. A. L. Sharpe et al., Science 365, 605–608 (2019).
20. M. Serlin et al., Science 367, 900–903 (2020).
21. Y. Xie et al., Nature 572, 101–105 (2019).
22. A. Kerelsky et al., Nature 572, 95–100 (2019).
23. Y. Jiang et al., Nature 573, 91–95 (2019).
24. Y. Choi et al., Nat. Phys. 15, 1174–1180 (2019).
25. M. I. B. Utama et al., Nat. Phys. 17, 184–188 (2021).
26. S. Lisi et al., Nat. Phys. 17, 189–193 (2021).
27. G. Chen et al., Nat. Phys. 15, 237–241 (2019).
28. D. N. Basov, R. D. Averitt, D. van der Marel, M. Dressel, K. Haule, Rev. Mod. Phys. 83, 471–541 (2011).
29. L. Ju et al., Science 358, 907–910 (2017).
30. See additional text and data in supplementary materials.
31. B. L. Chittari, G. Chen, Y. Zhang, F. Wang, J. Jung, Phys. Rev. Lett. 122, 016401 (2019).
32. Y. H. Zhang, D. Mao, Y. Cao, P. Jarillo-Herrero, T. Senthil, Phys. Rev. B 99, 075127 (2019).
33. M. Imada, A. Fujimori, Y. Tokura, Rev. Mod. Phys. 70, 1039–1263 (1998).
34. E. Dagotto, Rev. Mod. Phys. 66, 763–840 (1994).
35. W. Stephan, P. Horsch, Phys. Rev. B 42, 8736–8739 (1990).
36. H. C. Po, L. Zou, A. Vishwanath, T. Senthil, Phys. Rev. X 8, 031089 (2018).
37. C. Xu, L. Balents, Phys. Rev. Lett. 121, 087001 (2018).
38. Y. H. Zhang, T. Senthil, Phys. Rev. B 99, 205150 (2019).
39. J. van den Brink, M. B. J. Meinders, J. Lorenzana, R. Eder, G. A. Sawatzky, Phys. Rev. Lett. 75, 4658–4661 (1995).
40. J. Yang, Replication data for: Spectroscopy signatures of electron correlations in a trilayer graphene/hBN moiré superlattice (abg3036), Version 1. Harvard Dataverse (2022); https://doi.org/10.7910/DVN/LMBGXF.
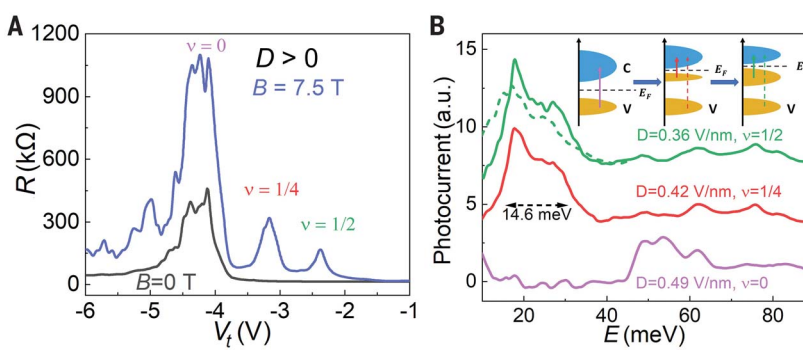
Fig. 4. Optical transitions in magnetic field–induced correlated insulating states. (**A**) Top gate–dependent device resistance at a fixed bottom-gate voltage $V_b = +38$ V. At zero magnetic field, a single resistance peak appears at filling factor $\nu = 0$. At $B = 7.5$ T, additional peaks appear at $\nu = \frac{1}{4}$ and $\frac{1}{2}$, corresponding to quarter- and half-fillings of the lowest conduction band. (**B**) Photocurrent spectra corresponding to the three resistance peaks at 7.5 T in (A). The $\nu = \frac{1}{4}$ and $\frac{1}{2}$ spectra are shifted by 3 and 6 a.u. respectively for clarity. At charge density $n = 0$, a peak centered at 50 meV indicates the optical transition across the main gap. At both $\nu = \frac{1}{4}$ and $\frac{1}{2}$, a peak centered at around ~22 meV appears, whereas the interband transition is merged into background. This low-energy peak mimics the peak in Fig. 3C (shown as a dashed curve for comparison) in both peak position and peak width, implying similar band-splitting physics as that in a Mott insulator. All the transport data in (A) and optical spectra in (B) are measured at 2 K.

SUPPLEMENTARY MATERIALS

science.org/doi/10.1126/science.abg3036
Methods
Supplementary Text
Figs. S1 to S11
References (*41–43*)

23 December 2020; accepted 16 February 2022
10.1126/science.abg3036